Materials Science & Engineering A 960 (2026) 150075

Contents lists available at ScienceDirect

Materials Science & Engineering A

journal homepage: www.elsevier.com/locate/msea

Strong and ductile additively manufactured Ti-6Al-4V through yttrium inoculation

Saeid Alipour [a,b,*], Ji Young Kim [c,b], Min Seok Kim [c,b], Arezoo Emdadi [a,**], Ju Li [b,***]

[a] Department of Materials Science and Engineering, Missouri University of Science and Technology, Rolla, MO, 65409, USA
[b] Department of Materials Science and Engineering and Department of Nuclear Science and Engineering, Massachusetts Institute of Technology, Cambridge, MA, 02139, USA
[c] Department of Materials Science and Engineering, Research Institute of Advanced Materials & Institute of Engineering Research, Seoul National University, Seoul, 08826, Republic of Korea

ARTICLE INFO

Keywords:
Additive manufacturing
Ti-6Al-4V
Grain structure control
Rare earth element
Inoculation
Strength-ductility

ABSTRACT

The unique microstructural features and thermal cycles in alloys produced by additive manufacturing (AM) techniques have led to the emergence of a new paradigm in the design and development of alloys for performance-critical applications. Despite the inherent microstructural features of AMed parts, optimizing the porosity-microstructure while acquiring desired mechanical performance has been crucial yet challenging. Hence, in many legacy alloys, achieving a strength-ductility synergy in the as-built condition without applying post-heat treatment or hybrid processes is considered an arduous task. In this research, we aimed to tailor the microstructure of the legacy Ti-6Al-4V alloy in the as-built condition by implementing the inoculation technique, as one of the recent techniques for microstructure control in AMed parts, to achieve an excellent combination of strength and ductility. Here, yttrium-rare earth element (REE) in its pure and oxide forms was used as an inoculant, which was decorated onto the Ti-6Al-4V alloy powder particles using the acoustic mixing method and, subsequently, the microstructure and mechanical properties of the directed energy deposited (DED) specimens were investigated. The FESEM, EBSD, and TEM microstructural investigations reveal that the Y and Y_2O_3 particles reacted in-situ during the printing process, leading to a distinct microstructure by forming new and dispersed precipitates. Specimens inoculated with the Y_2O_3, featuring a microstructure with plate-like and nearly equiaxed α phase and dispersed $(Y,Ti)_2O_3$ precipitates, exhibited uniform and excellent mechanical properties (e.g., UTS: ~1280 MPa and elongation: ~14%) in both horizontal and perpendicular directions in the as-printed condition. This research demonstrates that inoculation-based approaches can pave the way for achieving a strength-ductility synergy in as-built Ti-6Al-4V components with a minimal need for post-processing.

1. Introduction

Additive manufacturing (AM), a fundamental component of Industry 4.0, has shown significant adoption in recent years among many manufacturing techniques [1]. This significant rise is primarily ascribed to the distinctive attributes of additive manufacturing processes in fabricating components characterized by high complexity, reduced weight, and improved energy efficiency [2,3]. The primary advantages extend beyond these aspects; the distinctive microstructural attributes and thermal cycles intrinsic to the process result in alloys fabricated through various AM techniques, such as laser powder bed fusion (LPBF), wire arc additive manufacturing (WAAM), and directed energy deposition (DED) exhibiting micro and macro-structural features that markedly differ from those produced by traditional methods such as casting, rolling, and forging, despite having the same chemical compositions [4–6]. This phenomenon can be regarded as a double-edged sword for AMed components. This indicates that if the distinctive features of AM are not effectively utilized, they may not only fail to enhance the

* Corresponding author. Department of Materials Science and Engineering, Missouri University of Science and Technology, Rolla, MO, 65409, USA.
** Corresponding author.
*** Corresponding author.
E-mail addresses: saeid250@mit.edu (S. Alipour), emdadia@mst.edu (A. Emdadi), liju@mit.edu (J. Li).

https://doi.org/10.1016/j.msea.2026.150075
Received 29 December 2025; Received in revised form 5 March 2026; Accepted 7 March 2026
Available online 10 March 2026

performance of the printed component but could also result in premature failure by generating unwanted phases and phase heterogeneities in the as-built component [7]. Since balancing the porosity-microstructure-performance combination is frequently seen as a challenge, making it exceedingly difficult to attain the appropriate performance in the as-built condition [8,9]. Hence, AMed components are typically subjected to post-heat treatments or thermomechanical processes [10]. For instance, hybrid manufacturing procedures, such as the combination of rolling and AM, are utilized to achieve the desired microstructure and mechanical properties. However, such post-processing approaches often increase manufacturing complexity and cost [11–13].

Therefore, there has been growing interest in strategies that enable excellent mechanical properties solely through the AM process itself, without any post-processing heat treatments or mechanical deformation, by directly exploiting the intrinsic features of AM, namely the rapid solidification, steep thermal gradients, and in-situ thermal cycling, to tailor microstructure during printing [14]. For example, Rietema et al. demonstrated that in-situ large-area laser annealing during LPBF can be used to directly manipulate cooling rates and microstructural evolution in Ti-6Al-4V, thereby reducing the reliance on post-processing treatments [15]. In recent years, methods based on inoculation and minor chemical composition adjustments have garnered significant attention [16]. In these techniques, the addition of very small quantities of metallic or ceramic particles is intended to leverage the small melt pool size and unique solidification behavior of AM processes in a way that maximizes their effect on the microstructure and properties of as-built alloys [16,17]. The implementation of these methodologies has resulted in the development of a novel paradigm for alloy redesign in AM, exploiting the distinctive solidification and thermal cycling attributes of this process to attain desired microstructures and mechanical properties with minimal modifications [17–19]. In the case of titanium (Ti) alloy, numerous research has studied the impact of inoculants on the microstructural, mechanical, and corrosion properties. Ti-6Al-4V is regarded as the well-known legacy alloy among Ti alloys and has undergone substantial investigation concerning AM techniques such as LPBF, DED, and WAAM [20–22]. Despite the prevalent application of this alloy in fusion-based Ti alloy printing, adjusting printing parameters to attain an optimal microstructure with minimal phase heterogeneity and defects is a challenging task [20].

In many cases, although studies have reported achieving a minimal level of defects or anomalies in the as-built condition, the presence of columnar grains that span along the build direction is still observed [8,12]. The existence of such columnar grains with high texture, combined with phase heterogeneities, leads to premature mechanical failures in as-built specimens [23]. Numerous studies have investigated the effect of adding different inoculants, such as TiC [24], B_4C [25], ZrN [26], SiC [27], and TiN [26], into Ti-6Al-4V alloy feedstock which subsequently manufactured via AM. However, controlling the microstructure and achieving desirable mechanical properties with a strength-ductility synergy remains one of the main challenges. In many of the previous investigations, the use of inoculants has led to the formation of brittle and unwanted phases, or lack of microstructural control throughout the entire specimen which led a challenge in obtaining strength-ductility synergy [16,18]. Hence, in the current research, the effect of adding yttrium-rare earth element in its pure and well-known oxide form (Y_2O_3) was meticulously investigated with the aim of achieving superior mechanical properties. Here, the selected inoculants were decorated onto Ti-6Al-4V powder particles using the resonant acoustic mixing (RAM) technique, and subsequently, after DED process, the microstructure and mechanical properties of the as-built specimens were tested along different build directions.

2. Experimental methods

Gas-atomized Ti-6Al-4V ELI powder (grade 23) with the particle size range 45-106 μm (Carpenter Additive), pure yttrium (Alfa Aesar) and yttrium-oxide (American Elements) powder particles with the particle size range 200-800 nm were used in this work. A resonant acoustic mixer (LabRAM II, Resodyn) was implemented to mix the Ti-6Al-4V and 1 wt% Y/Y_2O_3 powders for 20 min. Additionally, simulations under both equilibrium and non-equilibrium conditions were performed using Thermo-Calc 2024b software with the TCTI: Ti-Alloys v5.1 database.

A customized powder-blown laser-directed energy deposition machine with 3-axis control was employed to fabricate wall and cuboid geometries on the wrought Ti-6Al-4V substrate. The printer included a Nd-YAG pulsed laser system, producing a peak output power of 1 kW, with a Gaussian intensity profile and a wavelength of 1070 nm. To ensure adequate adhesion between the initial layers and the substrate, the substrate was preheated using a laser power of 500 W and a scan speed of 200 mm/min, without powder flow. The initial four layers were deposited at a power of 500 W and a scan speed of 200 mm/min. Thereafter, the 90 layers were applied using a power of 450 W, a scanning speed of 200 mm/min, and a powder feed rate of 2.5 g/min. Argon shielding gas was used to prevent oxidation throughout the printing process. Grinding and polishing of printed Ti specimens were performed according to the recommended procedure by Struers company. A combination of OP-U and H_2O_2 (90%–10%) is employed in the final polishing stage to eliminate any titanium oxides. The metallographic samples were subsequently etched using Kroll's reagent to reveal the microstructure. The Hirox KH 8700 digital optical microscope and Helios Nanolab 600 microscope were implemented for light optical microscopy (LOM) and field emission scanning electron microscopy (FE-SEM) characterizations. The phase constitution was examined by electron backscatter diffraction (EBSD) with an acceleration voltage of 20 keV, assisted by analysis software (EDAX OIM, Oxford Aztec). The crystal structures for each sample were characterized by X-ray diffraction (XRD) using monochromatic Cu Kα radiation at room temperature, assisted by crystal structure visualization and diffraction simulation software (CrystalMaker & DiffCrystal). Scanning-transmission electron microscopy (S-TEM) observations were conducted using a Spectra 300 S-TEM Thermo Scientific apparatus operating at 200 kV. The lamella samples were prepared using a dual-beam SEM/Ga focused ion beam (FIB) instrument (FEI Helios 5 CX).

The tensile test specimens were extracted from deposited cubes using Sodick wire electrical discharge machining (wire EDM). A single rough cutting pass and three finishing passes were performed utilizing 0.3-mm diameter bronze wire, implementing a progressively decreasing material removal rate through decreased voltage and amperage to improve specimen dimensionality and lower the heat-affected zone. After the EDM cutting, heat-affected zones may appear on the external surface of specimens. Consequently, the specimens were polished using 600-grit, followed by 800-grit SiC sandpaper, and then washed with ethanol. The polishing process may lead to a minor change in the actual cross-section, typically marginally below the nominal values. To accurately measure tensile properties, a point micrometer was utilized to get three measurements of the actual gauge thickness and width, which were averaged to ascertain the true cross-sectional area of each specimen. Tensile testing of the tensile test specimens was conducted using a Tinius Olsen type 25ST with a 25-kN load cell. A strain rate of 0.25 mm/mm/min was applied for tensile specimen testing. Due to the relatively small gauge section size of tensile test specimens, an extensometer could not be mounted to each specimen; consequently, strains were assessed using the digital image correlation (DIC) approach. Six tensile specimens were evaluated at ambient temperature to get reproducible and reliable data.

3. Results and discussions

3.1. Feedstock preparation and characterization

A schematic of the acoustic mixing process is presented in Fig. 1a. This technique has recently been utilized for the uniform distribution of

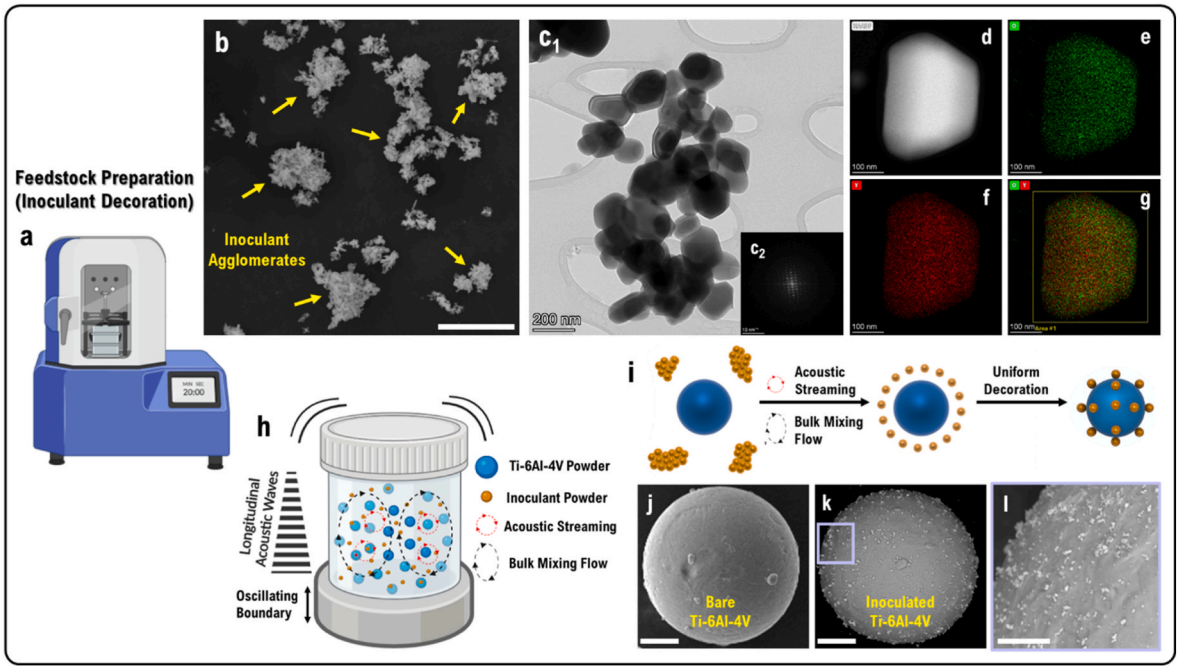

Fig. 1. (a) Schematic view of a resonant acoustic mixer (RAM) implemented for feedstock preparation, (b) SEM micrograph of agglomerated yttrium oxide (Y_2O_3) inoculant due to high van der Waals forces, (c_1, c_2) TEM micrograph and SAD pattern of Y_2O_3 inoculant particles, (d-g) HAADF and elemental map of an individual inoculant particle confirms the presence of yttrium and oxygen elements, (h, i) schematic representation of RM process illustrates the occurrence of bulk mixing flow and acoustic streaming generated by longitudinal acoustic waves resulting in uniform decoration of inoculant particles onto the surface of host particles, (j-l) low and high-magnification of bare and inoculated Ti-6Al-4V particles showing the uniform distribution of inoculant particles onto the host Ti-6Al-4V particles. Scale bar: (b) 10 μm (j, k) 15 μm, and (l) 2 μm.

ceramic and metallic materials which is an effective method for decorating powder particles ranging from 1 to 5 μm to a few nanometers [28]. An SEM micrograph of Y_2O_3 nanoparticles in Fig. 1b show the agglomeration as the main feature. This agglomeration is due to the inherent van der Waals forces that exist between the yttrium oxide nanoparticles. The bright field TEM (BF-TEM) micrograph of the Y_2O_3 nanoparticles reveals a morphology that is nearly spherical and irregularly polyhedral. This is confirmed by the selected area electron diffraction (SAED) pattern of the Y_2O_3 powder, as shown in Fig. 1c_2. Fig. 1d–g displays high-angle annular dark field (HAADF) and TEM-Energy dispersive X-ray spectroscopy (EDS) micrographs, also illustrate the chemical composition of the Y_2O_3 powder. Furthermore, the mechanism of acoustic mixing, which operates through longitudinal acoustic waves, is depicted in Fig. 1h. The presence of these waves leads to the generation of acoustic streaming and bulk mixing flow [29,30]. The process of deagglomerating the ceramic inoculant powders and their uniform distribution on the host Ti-6Al-4V particles is illustrated in Fig. 1i. Fig. 1j shows a micrograph of the bare Ti-6Al-4V before the acoustic process. Fig. 1k–l illustrate the acoustic mixed powder, clearly demonstrate the effective distribution of the inoculants on the surface of the host Ti-6Al-4V powder particles. At higher magnifications, it is evident that they are well-distributed and have formed a decent attachment. Such a uniform decoration is particularly critical in AM, where the melt pool is extremely small, and the thermal conditions vary rapidly between layers. Without homogeneous distribution at the feedstock stage, inoculants may agglomerate during deposition, leading to uneven nucleation and heterogeneous microstructures [31]. The RAM process, by providing bulk mixing flow and acoustic streaming help in dispersing of particles with subsequent decoration of Y/Y_2O_3 particles onto Ti-6Al-4V powder. Such a declaration can enhance their likelihood of contributing to in-situ reactions and heterogeneous nucleation during solidification.

Recently, the RAM method was employed for the development of GRX-810 powder [29]. In that application, a Ni-Co-Cr-based alloy was used as the host, and Y_2O_3 nano-particles served as the guest [30]. Due to the very small size of the melt pool, introducing inoculant particles with a decent initial distribution will aid in achieving a uniform distribution of the inoculant particles in the solidified layer right after deposition. Additionally, during the printing of subsequent layers, the sufficient distribution in the previous layer can ensure that the inoculant particles remain well-distributed.

3.2. *DED production and as-built specimens characterization*

The schematic of the DED process, alongside an illustration showing the layer-by-layer and track-by-track fabrication of cuboid samples using the DED nozzle shown in Fig. 2a. The light optical microscopy (LOM) microstructures of the as-built samples are displayed in Fig. 2b–d. In Fig. 2b, the microstructure is characterized by a basketweave morphology, which consists of needle-shaped alpha laths separated by thin layers of the beta phase. This formation is attributed to the comparatively high cooling rates during the AM process [20]. The microstructure in Fig. 2c, comprising alpha and beta structures with near-globular and plate-like alpha phases, indicates a different solidification scenario. Fig. 2d shows a microstructure similar to the basketweave pattern but with a very low fraction of plate-like alpha phases. Fig. 2e provides a schematic representation of the cutting plan for the tensile dog-bone specimens, designed to evaluate mechanical behavior in both horizontal and vertical orientations. This was intended to assess the uniformity, or homogeneity, of the mechanical response of the printed samples in different build directions. A customized specimen holder, engineered for testing the mini tensile dog-bone specimens, is shown in Fig. 2f. One of the primary challenges in obtaining accurate tensile property measurements is specimen slippage within the grips, which can lead to unreliable data [32]. To overcome this, a new fixture design was adopted. Although various specimen dimensions for characterizing the mechanical behavior of AMed specimens are proposed in the literature [32–34], the specific dimensions of the mini tensile test

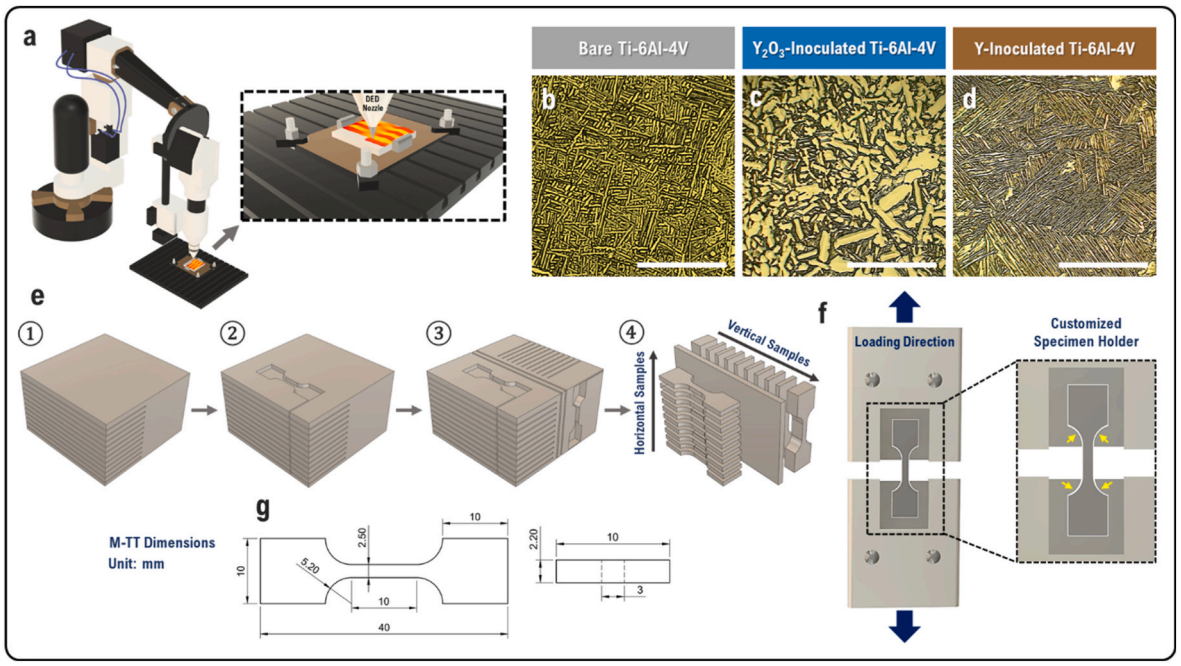

Fig. 2. (a) Schematic of DED process illustrating the cube specimen printing layer-by-layer and track-by-track, (b-d) LOM micrographs of as-built bare and inoculated Ti-6Al-4V specimens, (e) schematic representation of dog-bone samples extractions for horizontal and vertical tensile testing, (f) customized tensile specimen holder designed for the M-TT geometry, (g) designed M-TT specimen dimensions. Scale bar: (b-d) 100 μm.

dog-bone specimens used in this study are detailed in Fig. 2g.

3.3. Thermodynamic calculations (equilibrium and non-equilibrium)

Prior to microstructural examinations, thermodynamic predictions were employed as an attempt to identify the potential phases that could

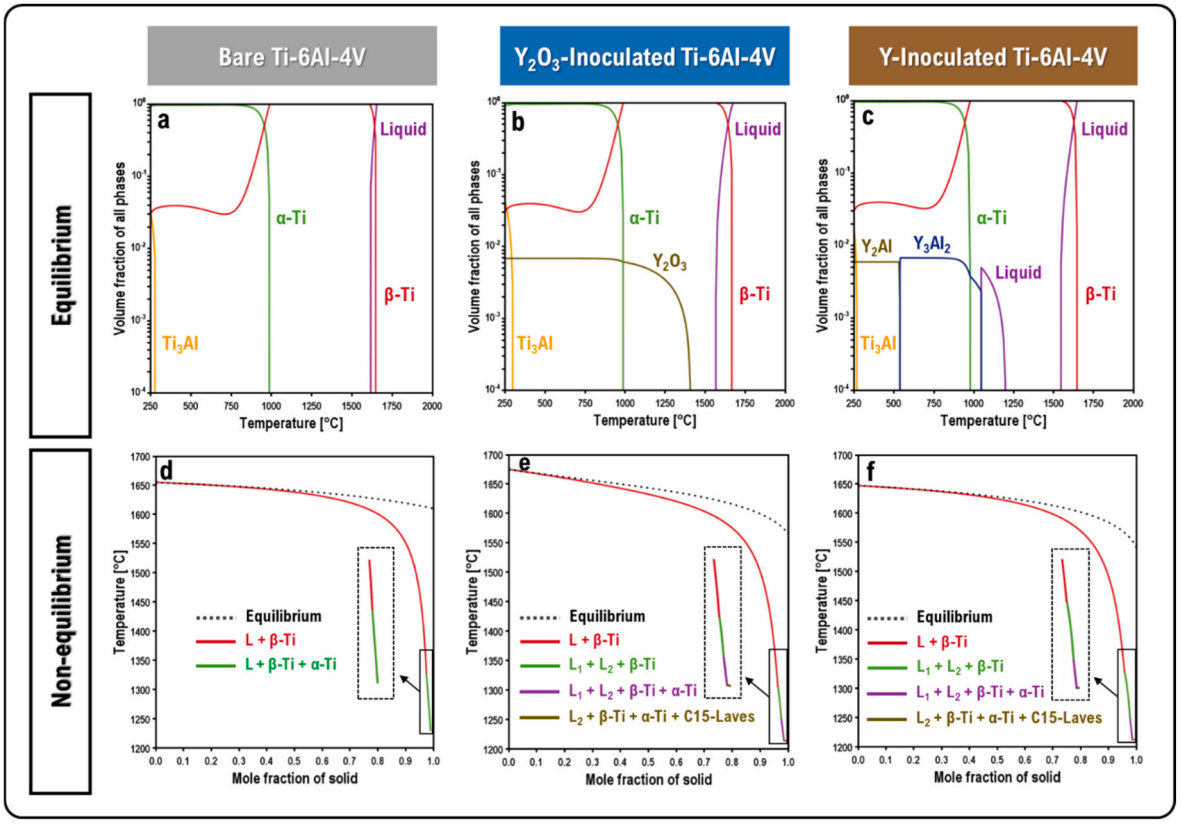

Fig. 3. Thermodynamic calculations of bare and inoculated Ti-6Al-4V alloys. (a-c) phase fraction diagrams simulating the equilibrium condition, (d-f) solidification pathway diagrams simulating the Scheil-Gulliver non-equilibrium condition.

form within the printed samples based on their different chemical compositions. Fig. 3a–c illustrate the phase fraction diagrams for the bare Ti-6Al-4V, yttrium-inoculated Ti-6Al-4V, and yttrium oxide-inoculated Ti-6Al-4V samples, respectively. Concurrently, Fig. 3d–f depict the solidification paths for these corresponding compositions. As shown in Fig. 3a, upon cooling from the liquid state, the β-titanium phase is the first to form. With continued cooling, all phases transform into β-titanium. Subsequently, as the temperature decreases further toward ambient conditions, a solid-state phase transformation occurs, converting the structure to α-titanium. A minor presence of the Ti_3Al phase is also predicted, the formation of which is contingent upon the solidification of the melt. The phase evolution depicted in Fig. 3b is analogous to that in Fig. 3a, with a key distinction: at approximately 1400 °C, the Y_2O_3 phase precipitates and remains stable down to room temperature. In Fig. 3c, the Y_3Al_2 phase forms at around 1100 °C; however, upon further cooling, it undergoes a solid-state transformation into the Y_2Al phase. Fig. 3d outlines the solidification path for bare Ti-6Al-4V, indicating the transformation from liquid to the β-titanium phase, followed by its solid-state transformation to α-titanium. For the yttrium-inoculated sample (Fig. 3e), the system transitions from the L+β-titanium region into a two-phase L_1+L_2+β-titanium region. Subsequently, β-titanium transforms into α-titanium, and ultimately, C15-Laves phases are formed. The solidification path for the yttrium oxide-inoculated Ti-6Al-4V, shown in Fig. 3f, proceeds similarly, exhibiting comparable behavior. It is important to note that the phases shown in the phase fraction diagrams (Fig. 3a–c) are predicted under the assumption of very slow, equilibrium cooling conditions. Under the non-equilibrium Scheil-Gulliver conditions, the phases formed differ from those at equilibrium (Fig. 3d–f). The solidification in the DED process is inherently non-equilibrium [20]. However, the complex thermal cycles imposed by the layer-by-layer and track-by-track deposition process complicate the thermal history during both solidification and subsequent high-temperature solid-state phase transformations [11]. The assumptions inherent in the Scheil-Gulliver solidification path model may lead to discrepancies between the predicted phases and those experimentally observed in the final microstructure of the as-built samples. Nevertheless, these predictions can clearly demonstrate that inoculant additions do not simply introduce new stable oxides or intermetallics in low temperature region but also modify the solidification sequences. Such changes are expected to influence heterogeneous nucleation events and grain refinement efficiency during DED, providing an underlying connection between the thermodynamic calculations and the experimentally observed microstructural differences. Furthermore, the discrepancy between predicted and observed phases emphasizes the necessity of considering rapid thermal cycling and repeated reheating inherent to AM processes, which cannot be fully captured by equilibrium or Scheil-based models alone.

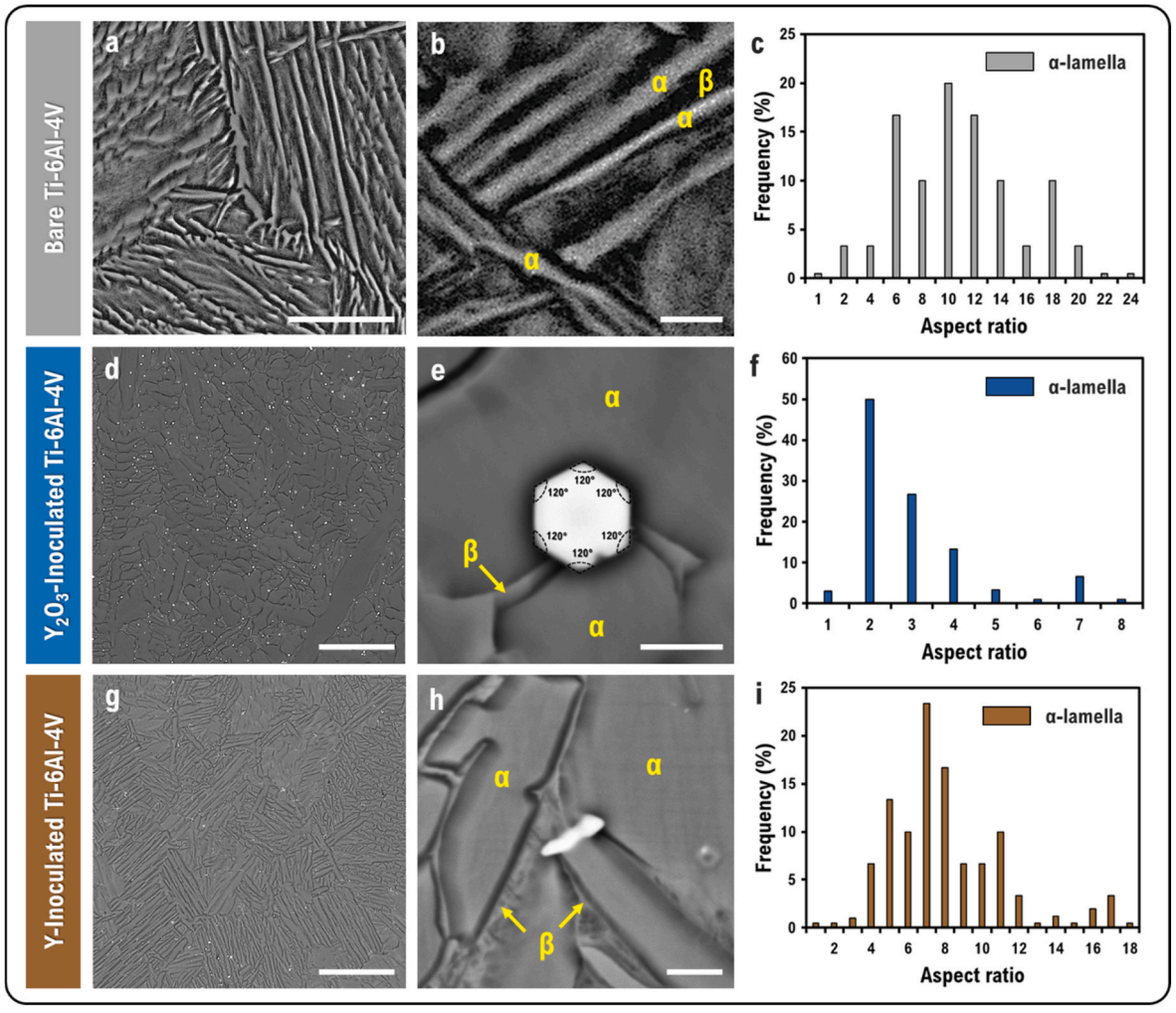

Fig. 4. FESEM of as-built bare and inoculated Ti-6Al-4V microstructures in (a, d, g) low magnification and (b, e, h) high magnifications along with the corresponding aspect ratio of α-lamella phase in (c, f, i). Scale bar: (a, d, g) 40 μm and (b, e, h) 2 μm.

3.4. Microstructural and phase characterizations

FESEM micrographs revealing the microstructure of as-built Ti-6Al-4V samples fabricated via the DED process are presented in Fig. 4a and b. As observed, the microstructure is characterized by a basketweave morphology, consisting of α and β lamellae, which is a typical feature of Ti-6Al-4V processed under high cooling rate conditions [20,35]. Fig. 4d and e displays the microstructure of the sample inoculated with Y_2O_3 (inoculated Ti-6Al-4V + Y_2O_3). This intervention has resulted in a completely different microstructure, featuring both plate-like and globular α phases. Furthermore, a uniform dispersion of white particles is evident throughout the microstructure. Many of these particles exhibit a regular morphology; notably, some present as perfect hexagons with 120° internal angles. The microstructure of the as-built samples inoculated with yttrium (inoculated Ti-6Al-4V + Y) are shown in Fig. 4g and h. This microstructure is distinct from both the un-inoculated and the Y_2O_3-inoculated samples. It is composed of needle-like alpha laths forming colonies with various orientations. White, elongated, and dispersed particles are also present within this microstructure. As was observed, the morphology of the alpha phase in the Y_2O_3-inoculated samples is distinctly different. Therefore, the alpha aspect ratio was calculated for the as-built bare and as-built inoculated Ti-6Al-4V samples, with the results presented in the images of Fig. 4i–f, and 4c. As the frequency distribution plot indicates, the alpha phase in the Y_2O_3-inoculated sample predominantly exhibits aspect ratios around 2 and 3. In contrast, the other samples show aspect ratios ranging from 7 to 12, which is indicative of elongated and needle-like alpha morphologies. This difference in morphology is likely due to different solidification behaviors and the distinct functionality of the added inoculants in the printed samples, a topic that will be further explored. These results suggest that the Y_2O_3 inoculants promote the formation of more equiaxed and globular α morphologies, which are generally associated with improved ductility by reducing stress concentration at α/β interfaces. In contrast, the elongated α lamellae observed in the bare and Y-inoculated samples are more likely to facilitate crack initiation and propagation along colony boundaries, thereby potentially influencing their strength–ductility balance. This is consistent with previous reports indicating that, although lamellar microstructures can provide high strength, they are often limited by reduced ductility and an increased tendency for crack initiation at α/β interfaces or colony boundaries [36,37]. Thus, the aspect ratio analysis provides a microstructural basis that may help rationalize the differences in mechanical behavior presented in the following sections. In addition to the microstructural characterization, the porosity of as-built specimens was measured from the representative cross-sectional FESEM images using image analysis (ImageJ). The measured porosity was 99.70%, 99.23%, and 99.45% for the bare Ti-6Al-4V, Y_2O_3-inoculated Ti-6Al-4V and Y-inoculated Ti-6Al-4V as-built specimens, respectively.

The X-ray diffraction (XRD) spectra for the yttrium- and Y_2O_3-inoculated samples are presented in Fig. 5a. As observed, the diffraction peaks primarily correspond to the α-titanium and β-titanium phases. The majority of the peaks are attributed to the α-titanium phase, which is consistent with the SEM and LOM micrographs shown in Figs. 2 and 4. A sharp peak corresponding to the (110) plane of β-titanium is evident at approximately $2\theta = 39°$. Two other low-intensity peaks for β-titanium are also detected: one corresponding to the (200) plane at $2\theta \sim 58°$ and another for the (211) plane at $2\theta \sim 73°$. Furthermore, a low-intensity peak is observed around $2\theta = 29.5°$ in the Y_2O_3-inoculated sample, which is shown at a higher magnification in Fig. 5b. This peak can be indexed to the (222) plane of the Y_2O_3 phase. It is noteworthy that the peaks corresponding to the bright phases observed in the micrographs in Fig. 4 are not clearly detectable. This can be attributed to the detection limit of the XRD technique, which makes it challenging to identify phases present in concentrations below approximately 1 wt%. As mentioned previously in the Materials and Methods section, the weight percentages of yttrium and Y_2O_3 used for inoculation were 1 wt%. Consequently, the bright phases formed are expected to be present in low weight fractions, hindering their diffraction and detection by XRD. Therefore, for more detailed microstructural investigations, EBSD and TEM analyses were employed, the results of which are presented in the subsequent sections.

As previously stated, the EDS-FESEM analysis was conducted for more precise microstructural characterization. Fig. 6 presents the FESEM image and corresponding EDS mapping for the Y_2O_3-inoculated sample. In Fig. 6a, point EDS analysis was performed on various regions, including the bright phases, α-titanium, and β-titanium. The table below the image details the mean and standard deviation (SD) of the measured compositions for these respective phases. Based on the measured values for Ti, Al, V, Y, and oxygen, the bright phases are likely the primary Y_2O_3 phase, with some of the yttrium atomic positions occupied by titanium atoms. Therefore, these bright phases can be represented as $(Y,Ti)_2O_3$ which were further identified with EBSD and TEM in the next sections.

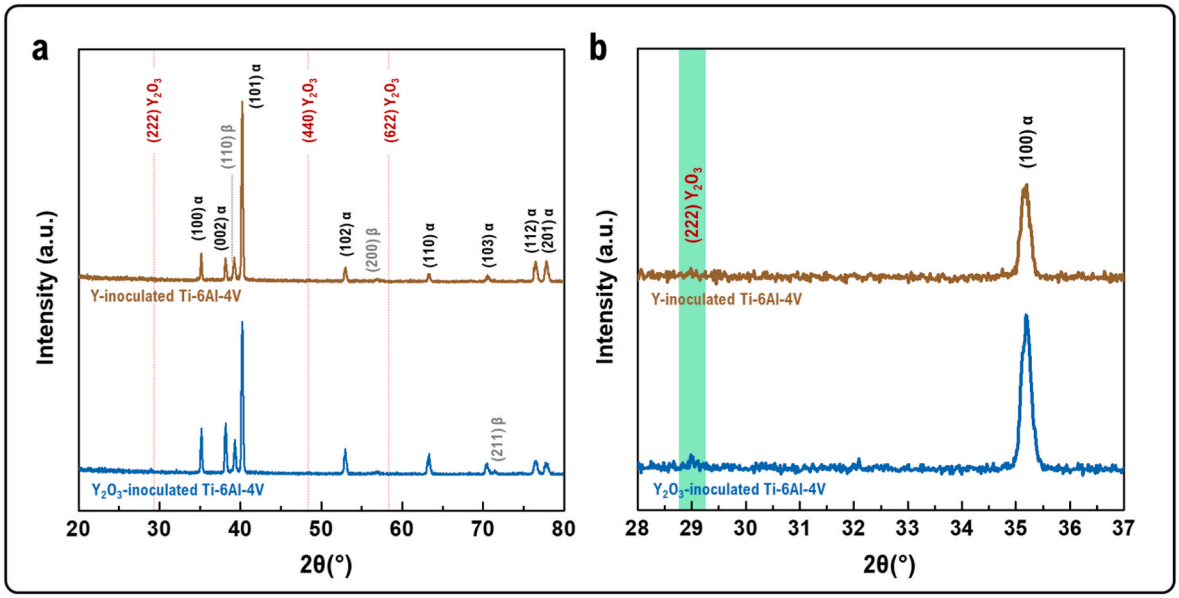

Fig. 5. XRD of as-built Y_2O_3-inoculated Ti-6Al-4V and Y-inoculated Ti-6Al-4V specimens, (a) overall spectrum and (b) detailed spectrum for $2\theta = 28\text{-}37°$ range.

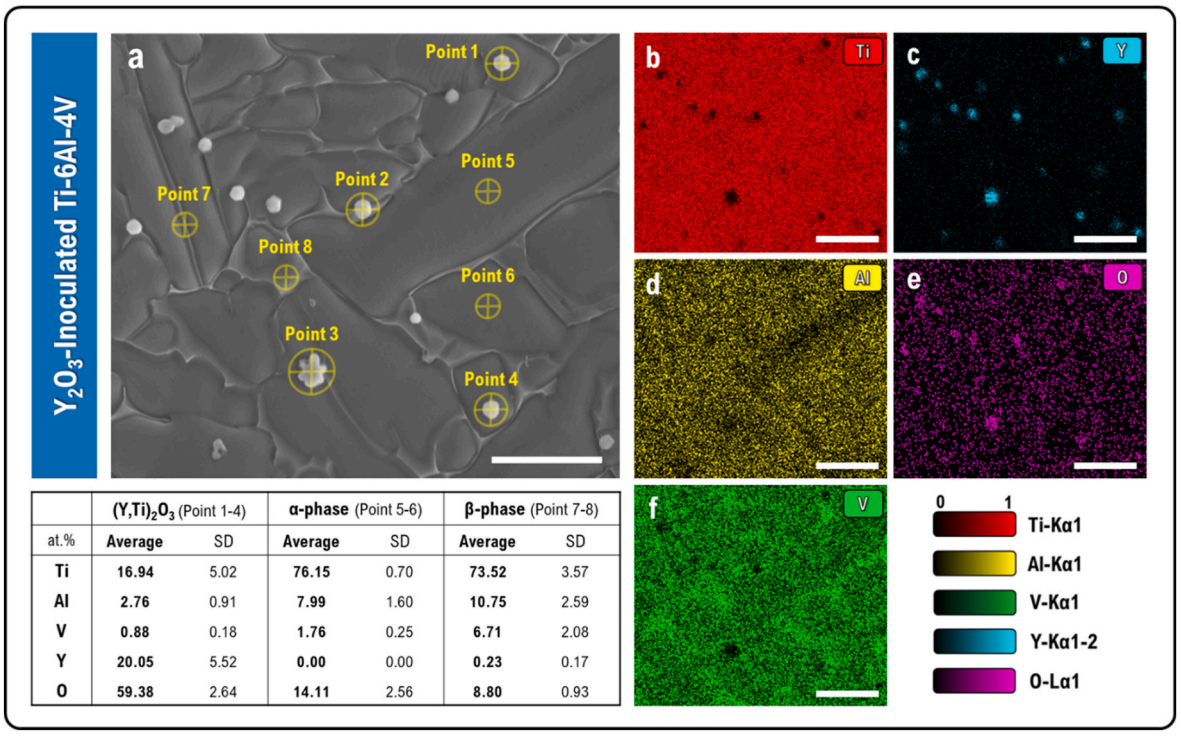

	$(Y,Ti)_2O_3$ (Point 1-4)		α-phase (Point 5-6)		β-phase (Point 7-8)	
at.%	Average	SD	Average	SD	Average	SD
Ti	16.94	5.02	76.15	0.70	73.52	3.57
Al	2.76	0.91	7.99	1.60	10.75	2.59
V	0.88	0.18	1.76	0.25	6.71	2.08
Y	20.05	5.52	0.00	0.00	0.23	0.17
O	59.38	2.64	14.11	2.56	8.80	0.93

Fig. 6. EDS-FESEM of as-built Y_2O_3-Inoculated Ti-6Al-4V microstructure. (a) SE images along with EDS elemental map for Ti, Al, V, Y, and O in (b-f). The EDS-point results are listed in the table for points 1-8 confirming the α-Ti, β-Ti, as well as $(Y,Ti)_2O_3$ phases. Scale bar: (a-f) 10 μm.

Other research has also identified complex phases of Ti, Y, and oxygen in the microstructures of samples produced under the non-equilibrium solidification conditions of LPBF and DED. The exact nature of these phases will be further investigated using EBSD and TEM. The analysis points 5, 6, 7, and 8 correspond to the α-titanium and β-titanium phases. The high oxygen content may be attributed to the oxygen present in the outer layer of the as-received Ti-6Al-4V powder from its manufacturing process, which can become entrapped within the melt pool during printing due to the high solidification rates [38]. Furthermore, the high reactivity of titanium makes oxygen pickup during the DED process an unavoidable occurrence. Elemental mapping, as shown in Fig. 6b–f, reveals the distribution of various elements. The bright regions within

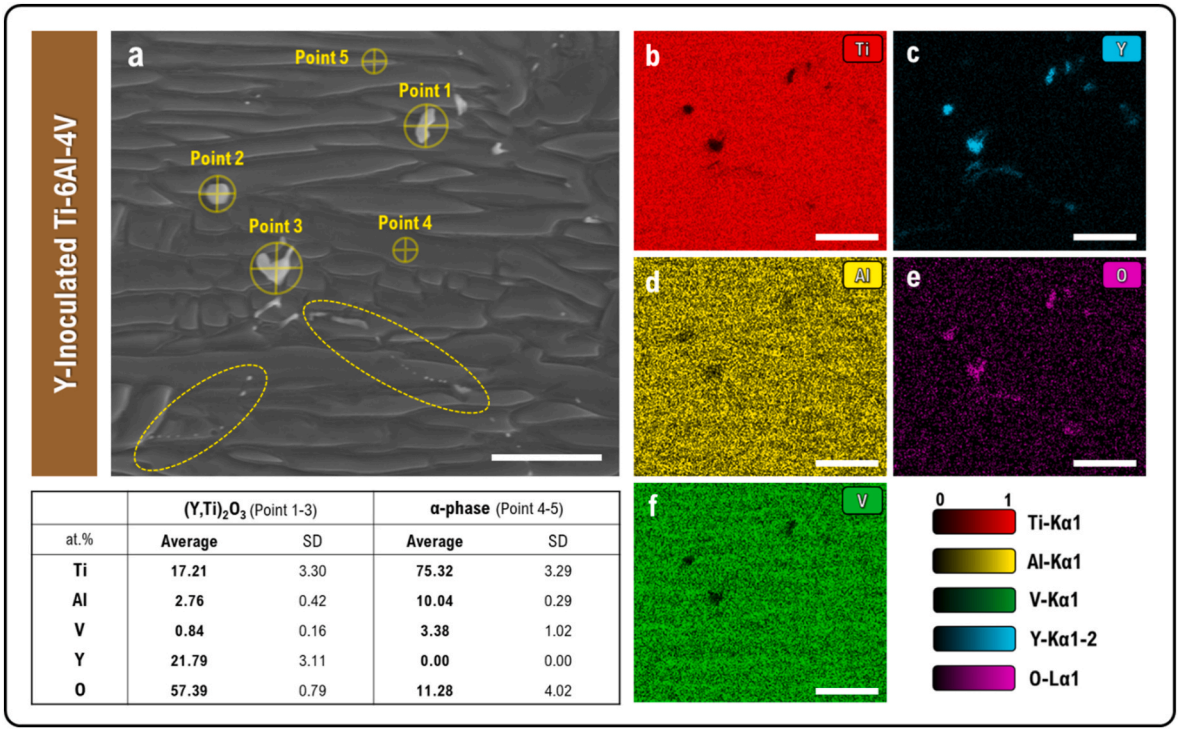

	$(Y,Ti)_2O_3$ (Point 1-3)		α-phase (Point 4-5)	
at.%	Average	SD	Average	SD
Ti	17.21	3.30	75.32	3.29
Al	2.76	0.42	10.04	0.29
V	0.84	0.16	3.38	1.02
Y	21.79	3.11	0.00	0.00
O	57.39	0.79	11.28	4.02

Fig. 7. EDS-FESEM of as-built Y-Inoculated Ti-6Al-4V microstructure. (a) SE images along with EDS elemental map for Ti, Al, V, Y, and O in (b-f). The EDS-point results are listed in the table for points 1-5 confirming the α-Ti and $(Y,Ti)_2O_3$ phases. Scale bar: (a-f) 10 μm.

the microstructure are predominantly composed of oxide-based Y_2O_3. The enrichment of the β-titanium phase regions with vanadium is due to its role as a β-stabilizer [32]. Furthermore, the enrichment of the α-titanium phase regions in aluminum is attributed to aluminum's function as an α-stabilizing element [32]. These concurrent enrichment of vanadium in β regions and depletion of aluminum in α regions reflects the classical partitioning behavior, confirming the reliability of the EDS data. Furthermore, The identification of $(Y,Ti)_2O_3$ indicates that the inoculant particles not only survive the high-temperature AM environment but also partially react with the Ti matrix, suggesting their thermodynamic stability and interfacial compatibility. Such phases can potentially act as heterogeneous nucleation sites for α during solidification, thereby modifying lamellar aspect ratios and promoting a more refined microstructure, as observed in subsequent analyses [39,40].

In a subsequent analysis, EDS-FESEM was performed on the yttrium-inoculated sample, with the results presented in Fig. 7. As shown in Fig. 7a, the bright phases in this image are characterized by a semi-continuous (intermittent) and elongated morphology. EDS point analysis of this sample indicates that these bright phases are rich in yttrium and oxygen, as well as titanium. Therefore, it is plausible that these phases are a form of Y_2O_3, where some of the yttrium sites are occupied by titanium atoms, resulting in a $(Y,Ti)_2O_3$ phase. As previously mentioned, this phase further identified with EBSD and TEM in the next sections. In contrast to the microstructure shown in Fig. 6, the alpha phases in this sample are more elongated and needle-like, and the β-titanium phase appears as very thin layers between the alpha laths. Points 1-3 correspond to the bright phases, which can be identified as $(Y, Ti)_2O_3$, while points 4 and 5 represent the needle-like alpha phase. The elemental maps for Ti, Al, V, Y, and O are shown in Fig. 7b–f. As is evident, the bright phases in the microstructure are predominantly enriched in Y and O. In contrast to Fig. 6, where globular or plate-like alpha phases were observed, this sample predominantly features needle-like alpha-titanium with minimal beta phase present. For this reason, the depletion of aluminum and the enrichment of vanadium in the elemental maps are not as distinctly discernible [32]. Due to the interaction volume from which the EDS point analysis signals are generated, the measured elemental compositions in the table may exhibit some deviation from the true values. Here, the elongated and semi-continuous morphology of the $(Y,Ti)_2O_3$ phase suggests that, unlike uniformly dispersed inoculant particles, these oxides are more likely to act as potential stress concentrators rather than efficient heterogeneous nucleation sites, thereby contributing to the needle-like α growth observed in this specimen. This observation highlights the importance of inoculant chemistry and distribution in determining whether the resultant particles function as effective nucleants or instead promote microstructural inhomogeneity. Therefore, more advanced microstructural analysis techniques are required for a detailed identification of the bright phases, which will be discussed in subsequent sections.

Various morphologies of in-situ formed oxide particles in the microstructure of as-built Y-Inoculated Ti-6Al-4V microstructure shown in Fig. 8a and b. As it shown, in addition to α-Ti and β-Ti, there are brighter phases with intermittent (Fig. 8a) or elongated (Fig. 8b)

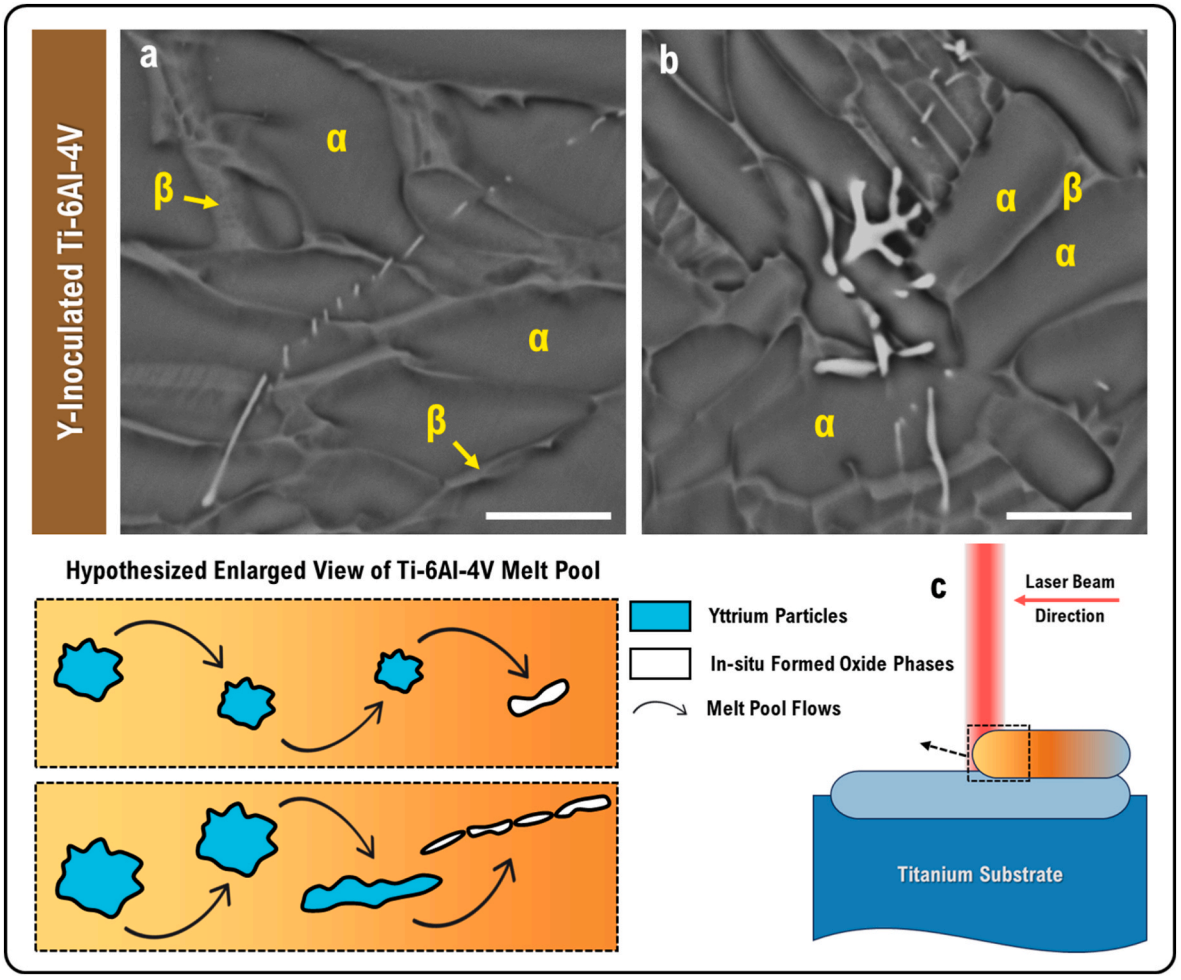

Fig. 8. (a,b) SE-FESEM of various morphologies of in-situ formed oxide phases in as-built Y-Inoculated Ti-6Al-4V microstructure, (c) schematic layer-by-layer deposition manner in DED process with the hypothesized enlarged view of Ti-6Al-4V melt pool, indicating the reactivity of yttrium particles to generate in-situ oxide phases similar to slags within the solidifying melt pool. Scale bar: (a, b) 3 μm.

features akin to slags. The observed features can be ascribed to the in-situ reaction of pure yttrium inoculant in the melt pool of DED Ti-6Al-4. In Fig. 8c, the hypothesized reaction mechanism of pure yttrium particles and forming the various morphologies of in-situ formed oxide phases is schematically illustrated. During the layer-by-layer deposition process and the presence of vigorous melt pool convection caused by the larger thermal gradient during DED process, the yttrium particles can gradually react with the Ti-6Al-4V melt pool and eventually form irregular-shaped oxide phases similar to slag morphologies [41]. In addition, the melt flow in the melt pool can cause some of the yttrium particles with larger sizes to progressively dissolve, resulting in intermittent, elongated oxide formation upon solidification. Unlike pre-dispersed Y_2O_3 particles that retain their integrity, pure Y inoculants experience significant dissolution and re-oxidation in the Ti-rich melt, which alter their morphologies. This elucidates why the resulting oxides act more as irregular slag inclusions rather than as efficient nucleation sites, ultimately promoting heterogeneous α growth along colony boundaries.

High-magnification EBSD analysis was conducted to investigate the nature of the phases formed within the microstructures of the inoculated Ti-6Al-4V samples. Fig. 9a presents a band contrast image of a region containing plate-like α-titanium, β-titanium layers, and a bright phase. The corresponding phase map in Fig. 9b reveals that the dominant, red-colored phase is α-titanium, while the green-colored β-titanium layers are situated between the α-titanium laths. The yellow-colored phase is identified as the cubic $(Y,Ti)_2O_3$ phase. Fig. 9d illustrates the BCC crystal structure of β-titanium and the HCP crystal structure of α-titanium. Further detailed investigation of the precipitated phases indicates that they are polycrystalline cubic structures. The pole figures for the α-titanium, β-titanium, and $(Y,Ti)_2O_3$ phases are shown in Fig. 9e. Due to the high magnification used for the EBSD scan, the pole figures exhibit textured regions, which is an expected outcome as they are constructed from the crystallographic orientations of a limited number of grains. Additionally, the Kernel Average Misorientation (KAM) map of printed microstructure shows a relatively low value in comparison to samples produced by LPBF which can be attributed to the lower cooling rates inherent to the DED process compared to LPBF [42]. Moreover, the relatively low KAM values can also suggest that the presence of inoculant-derived oxides did not significantly deteriorate the local lattice integrity.

Similarly, high-magnification EBSD analysis was conducted on the yttrium-inoculated Ti-6Al-4V + Y sample. The band contrast micrograph in Fig. 10a reveals a microstructure dominated by the α-titanium phase, with the β-titanium phase appearing as thin layers between the laths, distinguished by its darker contrast. Additionally, precipitated bright phases with an elongated morphology are evident in this image. The phase map of the microstructure shows the red-colored α-titanium phase, and the green-colored β-titanium lamellae situated between the alpha phases. Furthermore, the cubic $(Y,Ti)_2O_3$ phase is depicted in yellow. The HCP crystal structure for α-titanium and the cubic crystal structure for the $(Y,Ti)_2O_3$ phase are presented in Fig. 10d. In this sample as well, the KAM map is predominantly blue, with scattered green regions, which can be attributed to the relatively lower cooling rates of the DED process compared to LPBF [42,43]. The extremely high rates in LPBF processes typically result in KAM maps that are predominantly yellow and orange, indicating high levels of stored dislocations due to non-equilibrium solidification. The pole figure images for this sample also show discrete textured spots, reflecting the contribution of a limited number of phases to the pole figure construction, which is an expected result.

As previously discussed, TEM analysis was performed to identify the nature of the phases formed. For this purpose, lamellae were prepared from the as-built Ti-6Al-4V and the inoculated samples using a FIB technique. For the bare Ti-6Al-4V, the lamella was extracted from a random location. However, for the inoculated samples, the FIB trench was specifically targeted to a region containing a bright phase. As shown in the images in Fig. 11a and b, the targeted bright phase, indicated by the yellow arrow, was successfully captured within the FIB lamella. Following the thinning of the lamella, the α-titanium, β-titanium, and precipitated phases became observable, as shown in Fig. 11d_1-d_2, with α-titanium being the dominant phase. For the inoculated samples, TEM and SAED were employed to analyze the precipitates, which confirmed

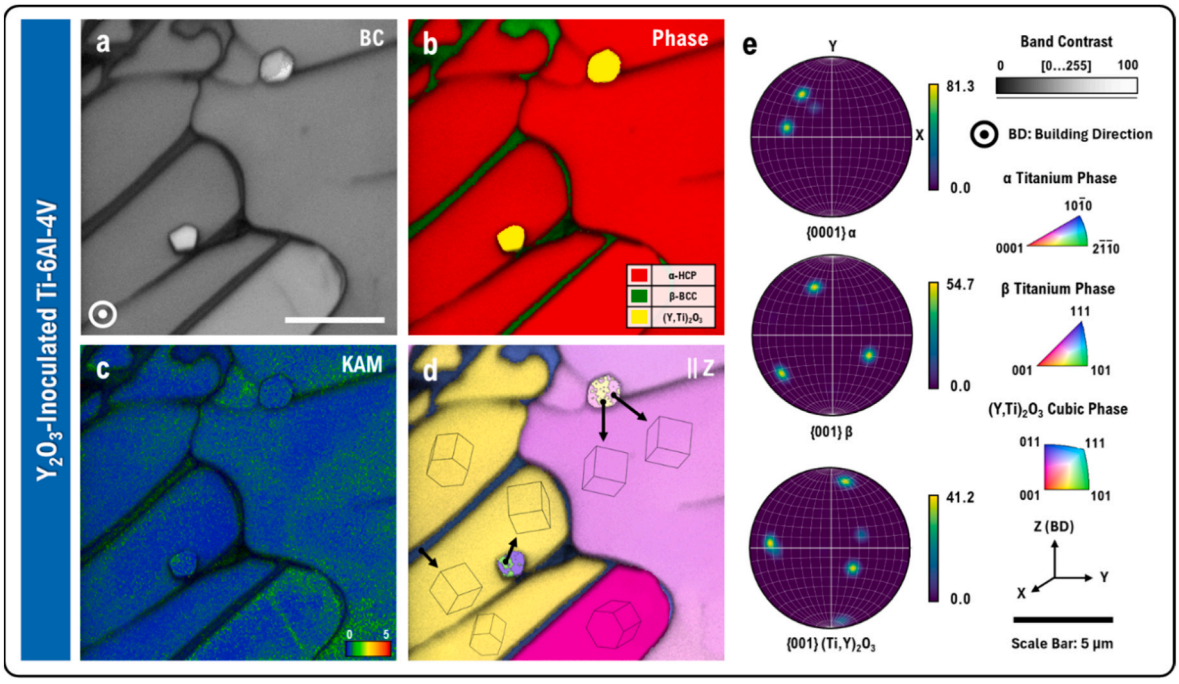

Fig. 9. EBSD of as-built Y_2O_3-inoculated Ti-6Al-4V microstructure. (a) band contrast, (b) phase map showing the α-HCP, β-BCC, and cubic $(Y,Ti)_2O_3$, (c) KAM map, (d) IPF image showing the crystallographic orientation of α-Ti, β-Ti, as well as polycrystalline $(Y,Ti)_2O_3$ phases, (e) corresponding pole figures map for α-Ti, β-Ti, and $(Y,Ti)_2O_3$ phases. Scale bar: (a-d) 5 μm.

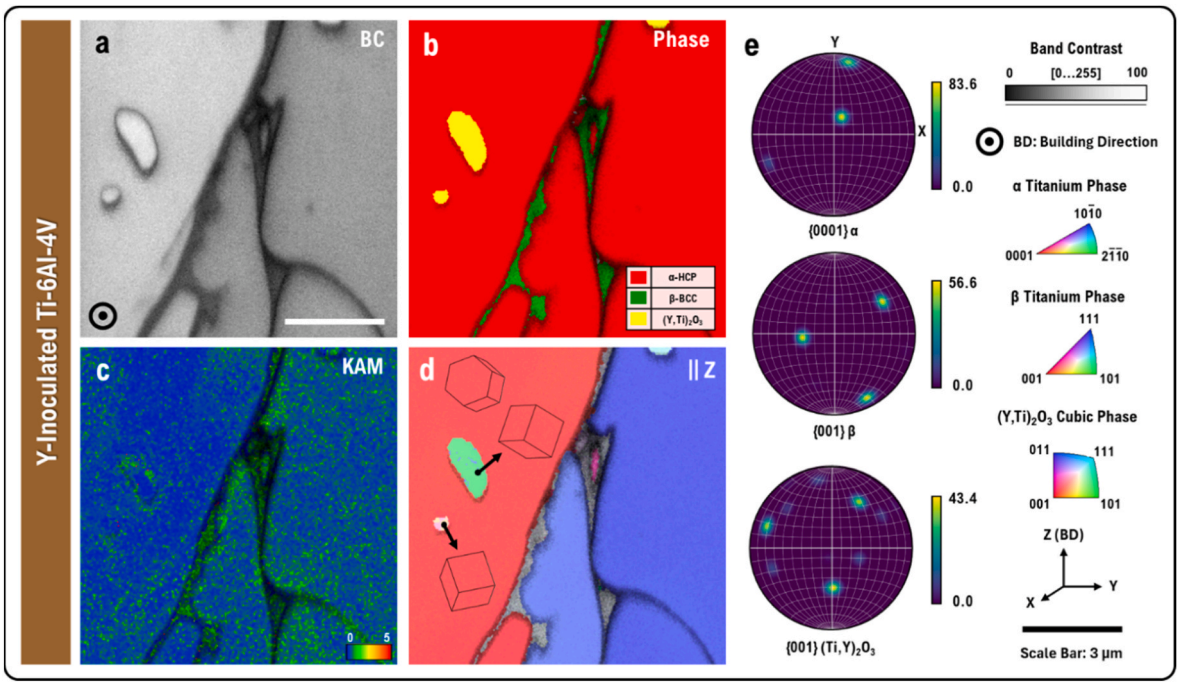

Fig. 10. EBSD of as-built Y-inoculated Ti-6Al-4V microstructure. (a) band contrast, (b) phase map showing the α-HCP, β-BCC, and cubic $(Y,Ti)_2O_3$, (c) KAM map, (d) IPF image showing the crystallographic orientation of α-Ti, β-Ti, as well as polycrystalline $(Y,Ti)_2O_3$ phases, (e) corresponding pole figures map for α-Ti, β-Ti, and $(Y,Ti)_2O_3$ phases. Scale bar: (a-d) 3 μm.

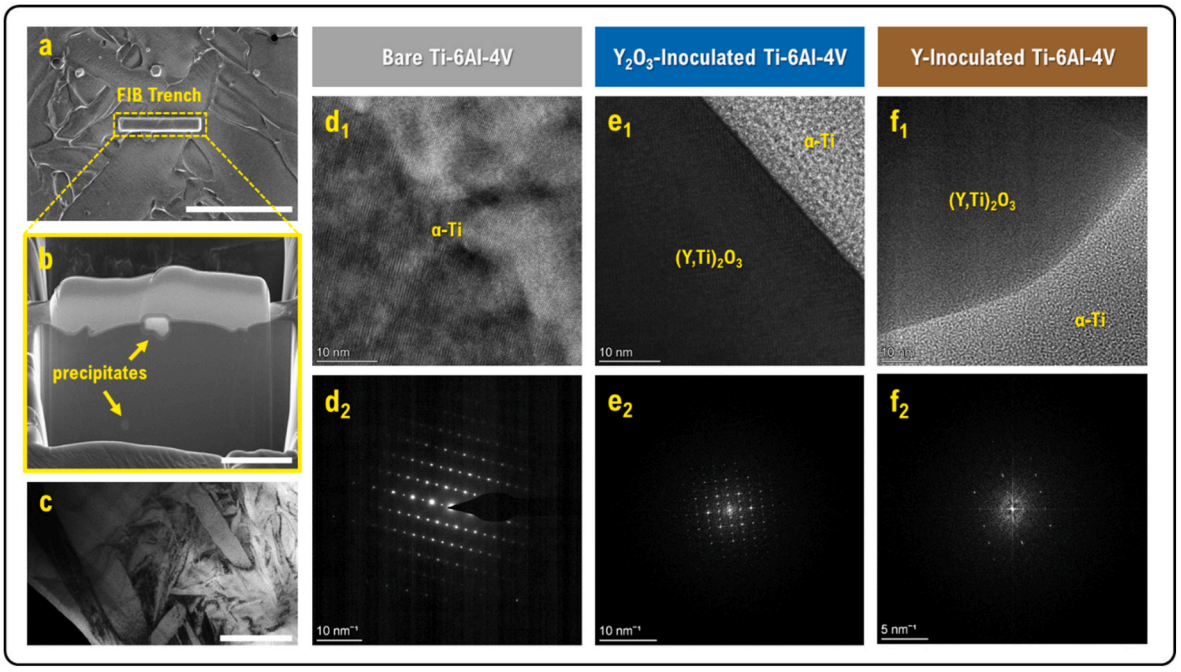

Fig. 11. TEM analysis of as-built microstructures: Bare-Ti-6Al-4V, Y_2O_3-inoculated Ti-6Al-4V, Y-inoculated Ti-6Al-4V. (a) area of interest for FIB trenching which contain bright precipitates, (b) lateral view of FIB lamella showing the target precipitates within the lamella, (c) the FIB lamella after ion thinning process, (d_1, e_1, f_1) HRTEM micrographs and (d_2, e_2, f_2) corresponding SAED pattern for bare and inoculated specimens. Scale bar: (a) 20 μm, (b) 5 μm, and (c) 1 μm.

the presence of the $(Y,Ti)_2O_3$ phase within the microstructure. High-resolution TEM and SAED confirm the presence of $(Y,Ti)_2O_3$ particles in direct contact with the α-Ti matrix.

3.5. Underlying mechanism

Based on the microstructural observations, a schematic illustrating the mechanism of precipitate formation in the printed samples has been hypothetically proposed in Fig. 12. During the additive manufacturing process, the sample is built layer by layer, and the presence of inoculant particles within the melt pool can lead to various transformations. In the case of the Y_2O_3-inoculated sample, the ceramic Y_2O_3 particles, when introduced into the Ti-6Al-4V melt pool, can undergo partial decomposition. This is due to the chemical reactions and the relatively

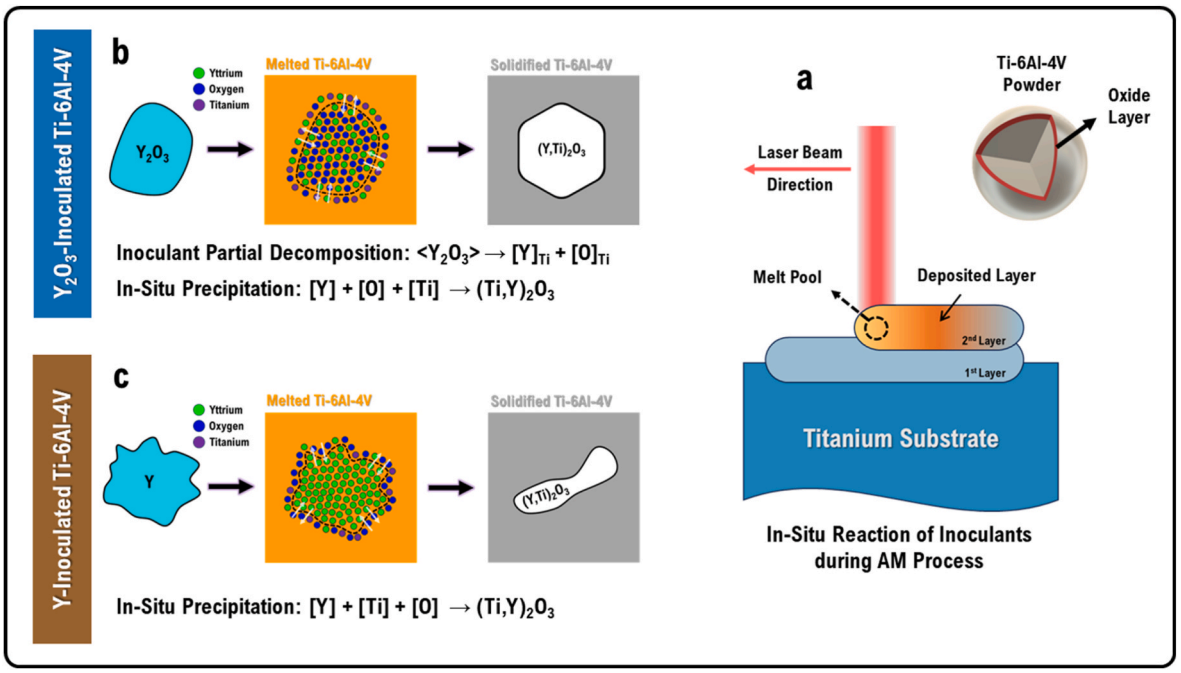

Fig. 12. Hypothesized underlying mechanism of microstructure control in REE-inoculated Ti-6Al-4V. (a) schematic representation of layer-wise production of DED process along with the Ti-6Al-4V as-received powder with intrinsic oxide layer on the surface. Schematic illustration for (b) in-situ partial decomposition of Y_2O_3 particles into Y and O in the melt pool and subsequent formation of $(Y,Ti)_2O_3$ precipitates, (c) in-situ reaction of pure Y in the Ti-6Al-4V melt pool and subsequent formation of $(Y,Ti)_2O_3$ slag-shaped precipitates. The oxide layer on the outer surface of as-received Ti-6Al-4V can mainly act as the source of oxygen for the precipitate formation.

sufficient time at high temperatures experienced during the DED process. Consequently, the Y_2O_3 particles can locally dissociate into yttrium and oxygen, which then disperse within the titanium melt pool. Simultaneously, due to its high reactivity, titanium has the potential to occupy some of the yttrium sites in the Y_2O_3 crystal structure. This leads to the formation of a $(Y,Ti)_2O_3$ phase with well-defined square, polyhedral, and hexagonal morphologies. Conversely, in the yttrium-inoculated sample, the pure yttrium phase, when exposed to the high local temperatures and the Ti-6Al-4V melt pool, can react with the titanium and the dissolved oxygen. This results in the formation of irregularly shaped and elongated $(Y,Ti)_2O_3$ phases. The oxygen required for this reaction is supplied by the intrinsic oxide layer on the surface of the Ti-6Al-4V powder particles. It is a common industrial practice for atomized spherical Ti-6Al-4V powders to have this intrinsic oxide layer to comply with safety and transportation regulations [44]. Furthermore, the strong affinity of yttrium for oxygen allows it to act as an oxygen scavenger within the melt pool. According to Ellingham diagram, the Gibbs free energy of formation for Y_2O_3 is significantly more negative than that for TiO_2 over the relevant temperature range of the DED process (1600°C-2800 °C). This indicates a much stronger affinity of yttrium for oxygen compared to titanium. As for the formation enthalpies, the standard enthalpy of formation (ΔH_f°) of Ti with O is calculated to be $TiO_2 \approx$-944 kJ/mol, whereas that of Y with O is $Y_2O_3 \approx$-1288 kJ/mol. As a result, yttrium preferentially scavenges oxygen in the melt pool, leading to the formation of Y-dominant oxides, with the partial substitution of Y lattice position by Ti as previously discussed. Regarding the differences in microstructure observed between the yttrium- and Y_2O_3-inoculated samples, the formation of globular and plate-like phases in the Y_2O_3-inoculated sample can be attributed to the action of partially dissolved Y_2O_3 particles as heterogeneous nucleation sites. Existing literature supports the role of ceramic Y_2O_3 particles as heterogeneous nucleation sites during the solidification process in AM [45]. In this context, the relatively lower cooling rates of the DED process compared to LPBF allow the partially melted Y_2O_3 phase sufficient time to promote the formation of thick beta phases, which subsequently transform into globular and shaped alpha phases during the solid-state phase transformation upon cooling. On the other hand, pure yttrium, with its lower melting point and stability compared to Y_2O_3, reacts with oxygen and titanium during the DED process. This reaction leads to the formation of Y-Ti-O slag-shaped precipitates in the final stages of solidification. Therefore, it is speculated that yttrium metallic phase does not primarily act as a heterogeneous nucleation site but rather dissolves first and then forms elongated slag-shaped precipitates in the later stages of solidification. This comparison underscores the importance of inoculant stability and thermodynamic robustness in determining whether added particles act as active nucleation sites or evolve into passive byproducts of the AM process. In order to definitively determine which mechanism is dominant, advanced in-situ techniques like synchrotron X-ray diffraction or imaging would be required. However, current limitations in synchrotron imaging for studying the precise reaction mechanisms and kinetics in such systems necessitate further investigation, which will be a focus of future research.

3.6. *Mechanical properties assessments*

The mechanical behavior of the as-built bare Ti-6Al-4V and the inoculated Ti-6Al-4V samples is presented in Fig. 13. The stress-strain curves for these samples are displayed in Fig. 13a. As indicated, the bare samples exhibit an Ultimate Tensile Strength (UTS) ranging from 1100 to 1150 MPa. However, these curves show significant scatter in elongation, which can be attributed to the phase heterogeneity of the as-built bare Ti-6Al-4V samples, a phenomenon previously reported in the literature [46]. In the yttrium-inoculated samples, both the Yield Strength (YS) and UTS values are increased, but this comes at the cost of reduced engineering strain, or ductility. The enhancement in YS and UTS in the yttrium-inoculated samples can be attributed to the presence of the semi-continuous and intermittent $(Y,Ti)_2O_3$ precipitates dispersed throughout the microstructure. The presence of these precipitates can increase strength via the Orowan strengthening mechanism [47]. However, as is evident, the ductility of these samples has decreased. This

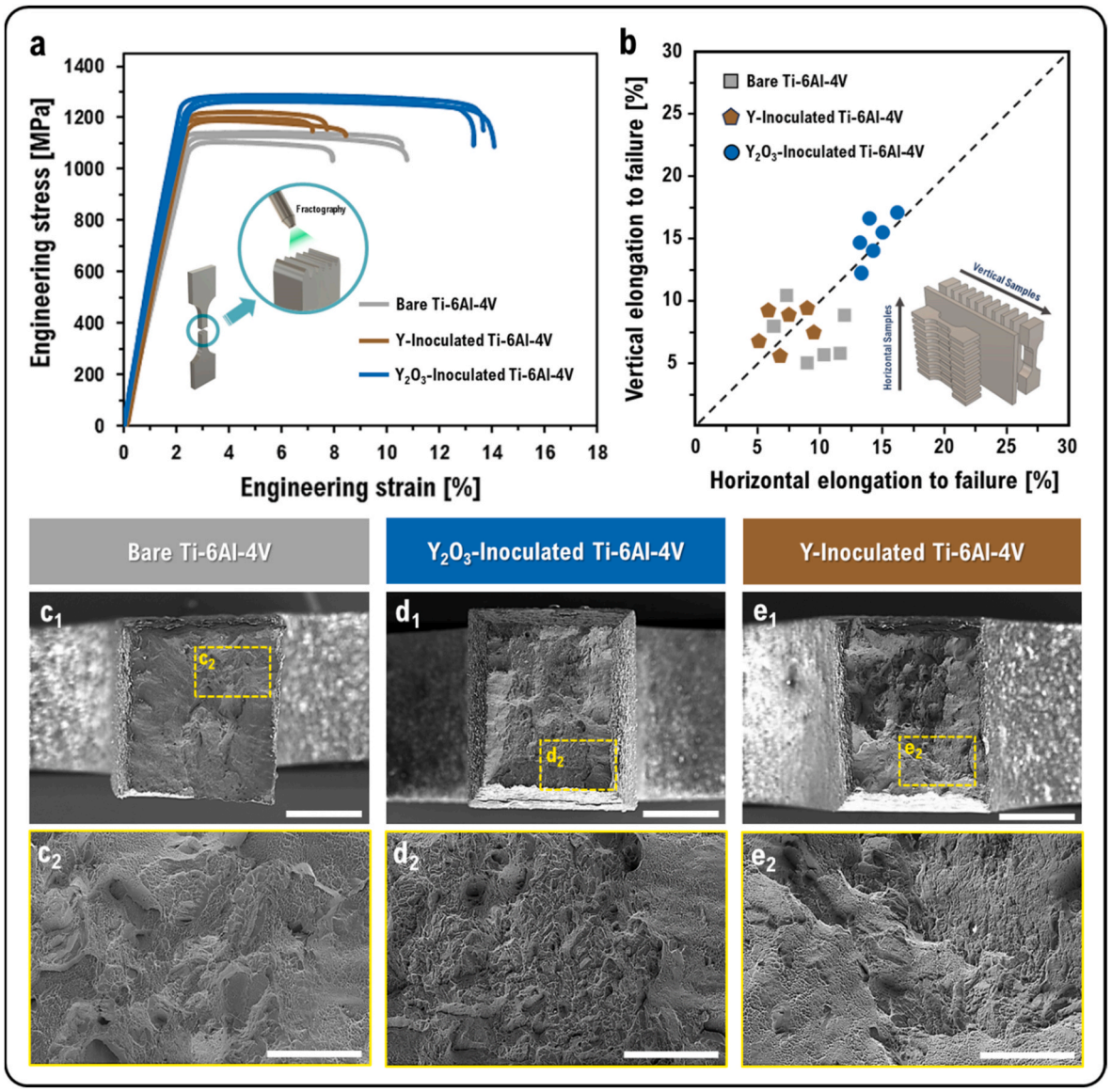

Fig. 13. Mechanical properties of as-built bare and REE-inoculated Ti-6Al-4V specimens. (a) Engineering stress-strain curves for bare and inoculated specimens, (b) horizontal versus vertical elongation to failure plot for assessing the homogeneity and consistency of resultant tensile properties in specimens tested parallel and perpendicular to building direction. Top fractography SE-FESEM images in (c_1, d_1, e_1) low magnifications and (c_2, d_2, e_2) high magnifications for bare and REE-inoculated specimens. Scale bar: (c_1, d_1, e_1) 800 μm and (c_2, d_2, e_2) 300 μm.

reduction in ductility can be attributed to the presence of elongated and relatively sharp $(Y,Ti)_2O_3$ precipitates within the microstructure. During crack initiation, these sharp precipitates with high aspect ratios can act as stress concentration sites, promoting crack propagation and leading to a failure to achieve low ductility [33,48].

In contrast, the sample inoculated with Y_2O_3 simultaneously exhibits high YS, UTS, and elongation. This superior strength-ductility synergy in the Y_2O_3-inoculated sample can be attributed to several factors. Firstly, the alpha phase in this sample has a lower aspect ratio compared to the other samples. As observed in Fig. 4c–f, and 4i, the alpha phase in this sample primarily consists of plate-like or globular morphologies, which is a stark contrast to the needle-like alpha structure seen in the bare Ti-6Al-4V and yttrium-inoculated samples. Various studies have shown that a microstructure with globular alpha phases, combined with α+β regions in other areas, leads to the attainment of high strength and ductility [49,50]. Secondly, the $(Y,Ti)_2O_3$ precipitates in this sample possess a regular and non-sharp morphology. This is in contrast to the yttrium-inoculated sample, where the absence of sharp-edged precipitates mitigates stress concentration and defect accumulation during loading. Furthermore, the microstructural observations of the Y_2O_3-inoculated sample reveal a uniform distribution of $(Y,Ti)_2O_3$ precipitates throughout the microstructure, without the presence of semi-continuous or intermittent regions. This uniformity is another factor contributing to the improved mechanical performance of this sample compared to the yttrium-inoculated one, which is a result of precipitation hardening. These results underscore that inoculant chemistry and stability play a decisive role in steering the phase transformation sequence and tailoring the resultant microstructure in a way that promotes superior properties. With appropriate selection, inoculants can act as highly effective nucleation sites and ensure a uniform, defect-resistant microstructure, thereby enabling significant improvements in the overall mechanical performance of additively manufactured Ti-6Al-4V.

Given that in most additively manufactured samples, mechanical behavior varies with direction [20,51], tensile dog-bone specimens were sectioned from both the horizontal and vertical orientations of the

cuboid samples for this study. Six dog-bone specimens were tested from each cube, with half oriented parallel and the other half perpendicular to the build direction of the cubes. The results are presented in Fig. 13b. As is evident, the bare Ti-6Al-4V sample exhibits the highest scatter with respect to the diagonal axes, indicating heterogeneity in the tensile behavior of the bare Ti-6Al-4V, which can be attributed to its non-uniform grain structure. The yttrium-inoculated sample shows relatively less scatter around the dashed line, a trend also observable in its stress-strain curves. The values measured for the Y_2O_3-inoculated sample, shown in blue in Fig. 13b, also exhibit relatively low scatter. This observation points to a greater homogeneity in tensile properties and a more consistent microstructure in the inoculated Ti-6Al-4V-Yttrium Oxide sample. More importantly, it indicates a mitigation of the strong anisotropy typically seen in AM Ti-6Al-4V, thereby ensuring more reproducible tensile properties across build orientations. Such consistency is critical for structural applications, as it might directly addresses long-standing concerns regarding property variability of AM components [52–54]. In addition, the suppression of columnar prior-β grain growth and the transition from coarse Widmanstätten lamellae to globular/plate-like α morphologies reduce the continuity of crystallographic variants and disrupt the development of strong prismatic texture in Ti-6Al-4V. The enhanced heterogeneous nucleation induced by Y_2O_3 further promotes orientation randomization during solidification and subsequent phase transformation. Together, these effects weaken the classical prismatic texture typically observed in additively manufactured Ti64 alloys, leading to the observed isotropic tensile behavior along horizontal and vertical directions.

Subsequently, top fractography images of the bare Ti-6Al-4V and inoculated Ti-6Al-4V samples were captured. As seen in Fig. 13c_1-c_2, the fracture surface is predominantly characterized by cleavage features in the surrounding areas and some ductile features in the central region. However, in the sample inoculated with Y_2O_3, the fracture surface displays shear regions around the neck and the central areas are mainly composed of fine dimples, indicating a relatively ductile fracture mode. For the yttrium-inoculated sample, as shown in Fig. 13e_1-e_2, the fracture surface predominantly consists of facets and cleavage with small regions of dimples. The observed fracture features can be correlated with the microstructures presented in Figs. 2 and 4 and 6–8. The microstructure of the Y_2O_3-inoculated sample, with its globular alpha structure, α+β phases, and a uniform and non-continuous distribution of $(Y,Ti)_2O_3$ throughout, exhibited a better strength-ductility synergy. The measured porosity values for the specimens (section 3.4) were relatively low and the difference between them were not significant, indicating that the observed differences in mechanical performance are not dominated by porosity variations.

4. Conclusions

In this research, REE inoculants were employed to control the microstructure of Ti-6Al-4V, aiming to achieve a tailored microstructure and superior mechanical properties. The key findings of this research can be summarized as follows:

- Yttrium REE in its pure and well-known oxide forms (Y_2O_3) was investigated for its effect on the microstructure of DED Ti-6Al-4V. The inoculant particles were uniformly decorated onto the Ti-6Al-4V powder particles using the RAM technique. This method ensured a highly uniform distribution with minimal agglomeration and contamination, thereby maximizing the inoculants' effect within the melt pool.
- Both of REE inoculants underwent in-situ chemical reactions during the printing process, transforming their chemical composition to $(Y,Ti)_2O_3$, albeit through different reaction mechanisms.
- The Y_2O_3 inoculant, following the printing process, induced a microstructure characterized by plate-like and globular alpha phases. It is speculated that these particles underwent in-situ reactions and acted as heterogeneous nucleation sites, resulting in their uniform dispersion throughout the microstructure.
- In contrast, the Y metallic phase inoculant, despite undergoing in-situ reactions, resulted in a completely different, non-uniform, elongated, and intermittent slag-shaped microstructure. This suggests that they did not effectively act as heterogeneous nucleation sites and instead influenced the microstructure in the final stages of solidification, with a less pronounced effect on the overall α/β morphology.
- The Y_2O_3-inoculated samples exhibited the best mechanical performance compared to the as-built bare and yttrium-inoculated printed samples. With a UTS of approximately 1300-1400 MPa and an elongation of ~16-18%, they demonstrated a synergistic strength-ductility behavior. This can be attributed to the globular/semi-equiaxed alpha-titanium and α+β lamellar microstructure, combined with the uniform distribution of equiaxed $(Y,Ti)_2O_3$ precipitates, which contribute to both grain refinement and precipitation strengthening.
- To assess the directional dependency of mechanical properties, samples were tested in both horizontal and vertical orientations. The Y_2O_3-inoculated samples exhibited the least scatter in their engineering strain values, indicating a more uniform microstructure and, consequently, more consistent mechanical properties.

CRediT authorship contribution statement

Saeid Alipour: Writing – review & editing, Writing – original draft, Visualization, Validation, Methodology, Investigation, Formal analysis, Data curation, Conceptualization. **Ji Young Kim:** Writing – review & editing, Writing – original draft, Investigation, Data curation. **Min Seok Kim:** Writing – review & editing, Writing – original draft, Investigation, Data curation. **Arezoo Emdadi:** Writing – review & editing, Writing – original draft, Visualization, Validation, Supervision, Project administration, Methodology, Investigation, Conceptualization. **Ju Li:** Writing – review & editing, Writing – original draft, Visualization, Validation, Supervision, Project administration, Methodology, Investigation, Conceptualization.

Declaration of competing interest

The authors declare that they have no known competing financial interests or personal relationships that could have appeared to influence the work reported in this paper.

Acknowledgments

We would like to express our gratitude to Dr. Jeremy Watts for his scientific and technical assistance. We acknowledge the facilities of the Material Research Center (MRC) and Peaslee Steel Manufacturing Research Center (PSMRC) at Missouri S&T university as well as the characterizations at MIT.Nano. Ji Young Kim and Min Seok Kim also acknowledge the support of Korean Institute for Advancement of Technology (KIAT) grant funded by the Korea Government (MOTIE) (RS-2024-00435406, Human Resource Development Program for Industrial Innovation (Global)). Ju Li acknowledges support by Framatome.

Data availability

Data will be made available on request.

References

[1] A. Haleem, M. Javaid, Additive manufacturing applications in industry 4.0: a review, Journal of Industrial Integration and Management 4 (4) (2019) 1930001.
[2] U.M. Dilberoglu, et al., The role of additive manufacturing in the era of industry 4.0, Procedia Manuf. 11 (2017) 545–554.

[3] A. Vafadar, et al., Advances in metal additive manufacturing: a review of common processes, industrial applications, and current challenges, Applied Sciences 11 (3) (2021) 1213.
[4] Z. Liu, et al., Additive manufacturing of metals: microstructure evolution and multistage control, J. Mater. Sci. Technol. 100 (2022) 224–236.
[5] D. Zhang, et al., Metal alloys for fusion-based additive manufacturing, Adv. Eng. Mater. 20 (5) (2018) 1700952.
[6] S. Alipour, et al., Recent advances toward damage-tolerant 3D-printed titanium alloys: alloy design perspective, J. Appl. Phys. 139 (4) (2026) 1–24.
[7] M. Brennan, J. Keist, T. Palmer, Defects in Metal Additive Manufacturing Processes, Springer, 2021.
[8] A. Mostafaei, et al., Defects and anomalies in powder bed fusion metal additive manufacturing, Curr. Opin. Solid State Mater. Sci. 26 (2) (2022) 100974.
[9] H. Taheri, et al., Powder-based additive manufacturing-a review of types of defects, generation mechanisms, detection, property evaluation and metrology, International Journal of Additive and Subtractive Materials Manufacturing 1 (2) (2017) 172–209.
[10] A. Diniță, et al., Additive manufacturing post-processing treatments, a review with emphasis on mechanical characteristics, Materials 16 (13) (2023) 4610.
[11] T. DebRoy, et al., Additive manufacturing of metallic components–process, structure and properties, Prog. Mater. Sci. 92 (2018) 112–224.
[12] S. Liu, Y.C. Shin, Additive manufacturing of Ti6Al4V alloy: a review, Mater. Des. 164 (2019) 107552.
[13] A. Malakizadi, et al., Post-processing of additively manufactured metallic alloys–A review, Int. J. Mach. Tool Manufact. 179 (2022) 103908.
[14] W. Xu, et al., In situ tailoring microstructure in additively manufactured Ti-6Al-4V for superior mechanical performance, Acta Mater. 125 (2017) 390–400.
[15] C. Rietema, et al., Microstructural control of additively manufactured Ti6Al4V via in-situ large-area laser annealing, Scr. Mater. 239 (2024) 115823.
[16] F.N. Lomo, et al., Advances in nano-inoculant grain refinement for fusion-based additive manufacturing of Al and Ti alloys, Mater. Des. (2025) 114581.
[17] Q. Tan, M. Zhang, Recent advances in inoculation treatment for powder-based additive manufacturing of aluminium alloys, Mater. Sci. Eng. R Rep. 158 (2024) 100773.
[18] D. Zhang, et al., Grain refinement of alloys in fusion-based additive manufacturing processes, Metall. Mater. Trans. 51 (9) (2020) 4341–4359.
[19] C. Wu, et al., Additive manufacturing of heat-resistant aluminum alloys: a review, Int. J. Extrem. Manuf. (2024).
[20] S. Alipour, et al., The trajectory of additively manufactured titanium alloys with superior mechanical properties and engineered microstructures, Addit. Manuf. 60 (2022) 103245.
[21] J. Su, et al., Recent innovations in laser additive manufacturing of titanium alloys, Int. J. Extrem. Manuf. 6 (3) (2024) 032001.
[22] J.-L. Su, et al., Laser additive manufacturing of titanium alloys: process, materials and post-processing, Rare Met. 43 (12) (2024) 6288–6328.
[23] I.P. Semenova, et al., Microstructure and mechanical properties of titanium alloys produced by additive technologies: new approaches and promising areas of research, Metals 14 (9) (2024) 966.
[24] C. Liu, et al., Additive manufacturing of (TiB+ TiC)/Ti6Al4V composites with tailored network reinforcement architecture, Compos. Commun. 40 (2023) 101611.
[25] S. Guo, et al., Microstructure and mechanical properties of Ti6Al4V/B4C titanium matrix composite fabricated by selective laser melting (SLM), J. Mater. Res. Technol. 23 (2023) 1934–1946.
[26] J.R. Kennedy, et al., The potential for grain refinement of wire-arc additive manufactured (WAAM) Ti-6Al-4V by ZrN and TiN inoculation, Addit. Manuf. 40 (2021) 101928.
[27] X. Li, et al., Effect of SiC addition on the microstructure and properties of Ti6Al4V by selective laser melting, J. Alloys Compd. 1010 (2025) 177330.
[28] M.R. Andrews, et al., Resonant acoustic® mixing: processing and safety, Propellants, Explos. Pyrotech. 45 (1) (2020) 77–86.
[29] T.M. Smith, et al., A 3D printable alloy designed for extreme environments, Nature 617 (7961) (2023) 513–518.
[30] T. Smith, et al., Efficient production of a high-performance dispersion strengthened, multi-principal element alloy, Sci. Rep. 10 (1) (2020) 9663.
[31] G. Karthik, H.S. Kim, Heterogeneous aspects of additive manufactured metallic parts: a review, Met. Mater. Int. 27 (1) (2021) 1–39.
[32] S. Alipour, et al., Implementation of miniature tensile specimens in mechanical properties assessment of directed energy deposited Ti-6Al-4V: as-Built and heat treated, Mater. Sci. Eng., A 921 (2025) 147593.
[33] J. Dzugan, et al., Mechanical properties characterisation of metallic components produced by additive manufacturing using miniaturised specimens, Virtual Phys. Prototyp. 18 (1) (2023) 2161400.
[34] N.M. Heckman, et al., Automated high-throughput tensile testing reveals stochastic process parameter sensitivity, Mater. Sci. Eng., A 772 (2020) 138632.
[35] F. Arias-González, et al., Microstructure and crystallographic texture of pure titanium parts generated by laser additive manufacturing, Met. Mater. Int. 24 (2018) 231–239.
[36] S. Zherebtsov, et al., Spheroidization of the lamellar microstructure in Ti–6Al–4V alloy during warm deformation and annealing, Acta Mater. 59 (10) (2011) 4138–4150.
[37] P. Ahmadian, M. Morakabati, The effect of lamellar and globular α-phase on mechanical behavior of strongly textured Ti–6Al–4V alloy, Trans. Indian Inst. Met. 73 (5) (2020) 1301–1309.
[38] P. Moghimian, et al., Metal powders in additive manufacturing: a review on reusability and recyclability of common titanium, nickel and aluminum alloys, Addit. Manuf. 43 (2021) 102017.
[39] Y. Watanabe, et al., Microstructure and strength of Ti-6Al-4V samples additively manufactured with TiC heterogeneous nucleation site particles, Materials 16 (17) (2023) 5974.
[40] Y. Watanabe, et al., 3D visualization of top surface structure and pores of 3D printed Ti-6Al-4V samples manufactured with TiC heterogeneous nucleation site particles, Metall. Mater. Trans. 51 (3) (2020) 1345–1352.
[41] J. Kennedy, et al., β grain refinement during solidification of Ti-6Al-4V in wire-Arc Additive Manufacturing (WAAM), in: IOP Conference Series: Materials Science and Engineering, IOP Publishing, 2023.
[42] M. Neikter, et al., Microstructural characterization and comparison of Ti-6Al-4V manufactured with different additive manufacturing processes, Mater. Char. 143 (2018) 68–75.
[43] J. Lee, et al., Comparative study on fatigue crack propagation behavior of Ti–6Al–4V products made by DED (direct energy deposition) and L-PBF (laser-powder bed fusion) process, J. Mater. Res. Technol. 23 (2023) 4499–4512.
[44] S.-K. Rittinghaus, B. Gökce, Safe production and processing of reactive powder materials in additive manufacturing, in: Safety Engineering: Fundamentals, Methods, Research Topics, Springer, 2025, pp. 175–196.
[45] L. Zhang, et al., Additive manufacturing of Y2O3-modified TA15 titanium alloy: enhanced mechanical properties at room and high temperatures: L. Zhang et al, Rare Met. (2025) 1–15.
[46] H. Zhao, Microstructure Heterogeneity in Additive Manufactured Ti-6Al-4V, The University of Manchester, United Kingdom, 2017.
[47] Z. Zhang, D. Chen, Contribution of Orowan strengthening effect in particulate-reinforced metal matrix nanocomposites, Mater. Sci. Eng., A 483 (2008) 148–152.
[48] X. Ren, et al., A comparative study on mechanical properties of Ti–6Al–4V alloy processed by additive manufacturing vs. traditional processing, Mater. Sci. Eng., A 817 (2021) 141384.
[49] M. Shunmugavel, A. Polishetty, G. Littlefair, Microstructure and mechanical properties of wrought and additive manufactured Ti-6Al-4 V cylindrical bars, Procedia Technol. 20 (2015) 231–236.
[50] M. Qian, et al., Additive manufacturing and postprocessing of Ti-6Al-4V for superior mechanical properties, MRS Bull. 41 (10) (2016) 775–784.
[51] B. Dutta, F.H.S. Froes, The additive manufacturing (AM) of titanium alloys, in: Titanium Powder Metallurgy, Elsevier, 2015, pp. 447–468.
[52] T. Vilaro, C. Colin, J.-D. Bartout, As-fabricated and heat-treated microstructures of the Ti-6Al-4V alloy processed by selective laser melting, Metall. Mater. Trans. 42 (10) (2011) 3190–3199.
[53] B.E. Carroll, T.A. Palmer, A.M. Beese, Anisotropic tensile behavior of Ti–6Al–4V components fabricated with directed energy deposition additive manufacturing, Acta Mater. 87 (2015) 309–320.
[54] S. Wolff, et al., Anisotropic properties of directed energy deposition (DED)-processed Ti–6Al–4V, J. Manuf. Process. 24 (2016) 397–405.